

SG1120-1202: MASS-QUENCHING AS TRACKED BY UV EMISSION IN THE GROUP ENVIRONMENT AT $z = 0.37$

JONATHAN T. MONROE

Physics and Astronomy, Texas A&M University, College Station, TX 77840, USA

KIM-VY H. TRAN

Physics and Astronomy, Texas A&M University, College Station, TX 77840, USA

AND

ANTHONY H. GONZALEZ

Astronomy Department, University of Florida, Gainesville, FL 32611, USA

Draft version February 5, 2022

ABSTRACT

We use the *Hubble Space Telescope* to obtain WFC3/F390W imaging of the supergroup SG1120-1202 at $z = 0.37$, mapping the UV emission of 138 spectroscopically confirmed members. We measure total (F390W–F814W) colors and visually classify the UV morphology of individual galaxies as “clumpy” or “smooth.” Approximately 30% of the members have pockets of UV emission (clumpy) and we identify for the first time in the group environment galaxies with UV morphologies similar to the jellyfish galaxies observed in massive clusters. We stack the clumpy UV members and measure a shallow internal color gradient, which indicates unobscured star formation is occurring throughout these galaxies. We also stack the four galaxy groups and measure a strong trend of decreasing UV emission with decreasing projected group distance (R_{proj}). We find that the strong correlation between decreasing UV emission and increasing stellar mass can fully account for the observed trend in (F390W–F814W)– R_{proj} , i.e., mass-quenching is the dominant mechanism for extinguishing UV emission in group galaxies. Our extensive multi-wavelength analysis of SG1120-1202 indicates that stellar mass is the primary predictor of UV emission, but that the increasing fraction of massive (red/smooth) galaxies at $R_{\text{proj}} \lesssim 2R_{200}$ and existence of jellyfish candidates is due to the group environment.

Subject headings: galaxies: clusters: individual (SG1120-1202) - galaxies: evolution - galaxies: star-burst - galaxies: morphology

1. INTRODUCTION

How galaxies evolve as a function of their local environment continues to be a rich topic of exploration for both observational and theoretical studies. The origins of well-established trends such as the increasing fraction of blue/star-forming/disk-dominated galaxies in galaxy clusters at higher redshift (e.g. Butcher & Oemler, A. 1978; Dressler 1980; Stanford et al. 1998; Cooper et al. 2010) seem to be rooted in environmental processes. However, dissecting the relative importance of physical mechanisms such as ram pressure stripping (Gunn & Gott III 1972; Abadi et al. 1999), galaxy harassment (Moore et al. 1998), tidal interactions (Byrd & Valtonen 1990), and gas starvation (Larson et al. 1980; Bekki et al. 2002) remains a challenge.

In the hierarchical formation model (Peebles 1970), galaxy clusters are built by merging smaller groups. Observations of nearby groups show they have more in common with galaxy clusters than with the field population, i.e., higher early-type fractions and lower mean star-formation rates than the field (Hashimoto et al. 1998; Zabludoff & Mulchaey 1998; Tran et al. 2001), and observations at $z \gtrsim 0.2$ highlight the importance of the group environment in transforming late to early-type galaxies (Gallazzi et al. 2009; Iovino et al. 2010; Koyama et al. 2010).

Motivated by the rapid evolution of the spiral population since $z < 1$ (Dressler et al. 1997; Kodama et al. 2001; Postman et al. 2005; Wilman et al. 2008), many investigations focus on the transformation of infalling spirals, either via a rapid, triggered burst of star formation or quenching of subsequent star formation. Simulations are sufficiently advanced that new insight can be obtained by, e.g. comparing star-forming regions and gas-loss rates to observations (Tonnesen et al. 2007). Also, galaxy mass may have a more dominant role in quenching star formation when clusters are still assembling (Peng et al. 2010; Muzzin et al. 2012), i.e., when galaxies are in a more group-like environment. However, to connect galaxies evolving in groups to more massive clusters requires identifying the progenitors of local clusters, i.e., galaxy groups at higher redshift.

The supergroup SG1120-1202 (hereafter SG1120) at $z = 0.37$ provides a unique laboratory for studying galaxies in a group environment before the groups merge to form a more massive galaxy cluster. SG1120 was discovered in the Las Campanas Deep Cluster Survey (Gonzalez et al. 2001) and is composed of four X-ray luminous galaxy groups that will merge to form a cluster comparable in mass to Coma (Gonzalez et al. 2005). Our extensive multi-wavelength observations show that most of SG1120’s members have early-type morphologies ($> 60\%$; Kautsch et al. 2008) and that most of the S0 members formed before the cluster phase (Just et al.

2011). However, the fraction of members that are bright $24\mu\text{m}$ sources is nearly as high as in the field ($\sim 30\%$ Tran et al. 2009). Spectroscopy with integral field units also show that several SG1120 members have outflowing winds that may aid in quenching star formation (Free-land et al. 2011).

In this paper, we focus on current star formation as traced by UV emission using *Hubble Space Telescope* imaging with WFC3/F390W. By combining with our existing ACS/F814W mosaic, we obtain high-resolution color maps of the supergroup members to pinpoint (dust-free) star-forming regions and measure internal color gradients. We compare the UV maps to stellar masses and projected group distance to quantify the relative importance of mass versus environmental quenching. Throughout the paper, we use $H_0 = 70 \text{ km s}^{-1} \text{ Mpc}^{-1}$, $\Omega_M = 0.3$ and $\Omega_\Lambda = 0.7$. At $z = 0.37$, this corresponds to a scale of $5.12 \text{ kpc arcsec}^{-1}$ and a look-back time of 4 Gyr.

2. OBSERVATIONS

Gonzalez et al. (2005) identified a merging system of four X-ray luminous groups with a total combined mass of $5.3 \times 10^{14} M_\odot$ (hereafter called SG1120; see Table 1 for SG1120 properties). The individual galaxy groups lie on the local $\sigma - T$ relation, and a virial analysis using their X-ray masses and relative locations indicates that these groups are bound to each other, likely infalling for the first time, and will merge into a single system by $z = 0$. A weak-lensing analysis based on HST imaging supports this picture (Smit et al. 2015), and 174 group galaxies have been spectroscopically confirmed using Magellan, MMT, and VLT/VIMOS.

Previous studies comparing SG1120 to clusters have found comparable fractions of early-type members (Kautsch et al. 2008) but also enhanced fractions of $24\mu\text{m}$ sources (Tran et al. 2009). The high fraction of early-type galaxies combined with enhanced star formation in SG1120 indicates that the transition to the cluster environment is well underway even in the group environment. The combination of cluster and field-like properties make SG1120 a unique laboratory for investigating how environmental processes drive and/or quench star formation.

2.1. Hubble Space Telescope Imaging

We employ HST imaging of an $\sim 8' \times 12'$ mosaic across three filters: F390W (WFC3/UVIS), F606W (ACS/WFC), and F814W (ACS/WFC) for a total of 44 pointings (combined primary and parallels) during cycles 14 (GO 10499) and 19 (GO 12470). The exposure times in F814W and F390W were 2000 s and 2610 s, respectively. At $z = 0.37$, these three filters probe rest-frame UV and optical emission to track both recent star formation and the existing stellar population. Furthermore, the high resolution of HST/WFC3 resolves the internal structure and the fine details of the individual galaxies. We measure galaxy sizes (radii) using F814W and use F390W to identify compact star-forming regions. The F606W is only used to generate the color images for a subset of members; the F606W coverage is not as extensive as F390W and F814W (see Fig. 1).

Of the original sample of 174 spectroscopically confirmed members, we exclude 31 because they do not have imaging in either F814W or F390W. Furthermore, eight

galaxies fall near boundaries on the CCD and so our measurements are unreliably noisy, leaving a total of 136 confirmed supergroup galaxies for which we can measure galaxy colors and visually classify their F390W emission. For details on the spectroscopy and stellar mass measurements from multi-band ground-based observations, we refer the reader to Tran et al. (2009).

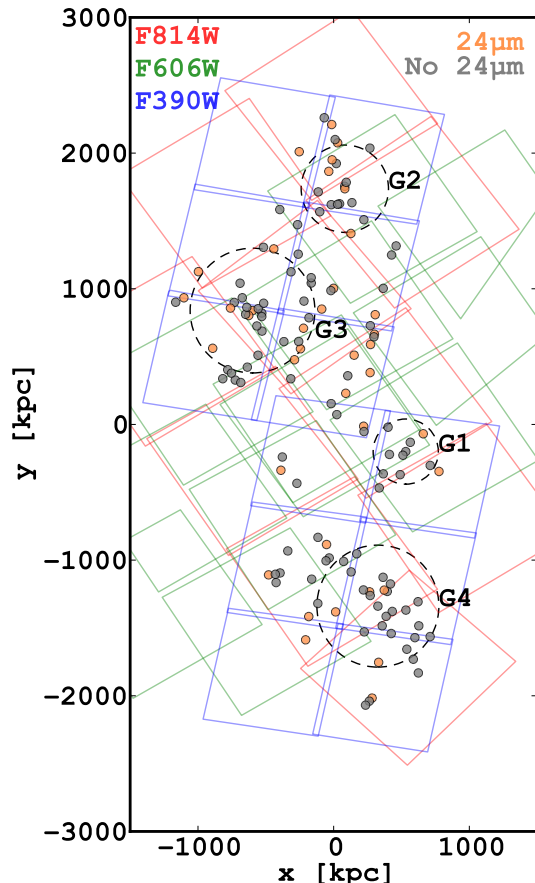


FIG. 1.— Spatial distribution of spectroscopically confirmed members across the entire galaxy supergroup SG1120-1202; north is up and east is to the left. HST coverage in WFC3/F390W, ACS/F606W, and ACS/F814W are included in blue, green, and red, respectively. MIPS $24\mu\text{m}$ detection or non-detection is denoted with orange or gray color, respectively. Black dashed circles of radius R_{200} are centered on each Brightest Group Galaxy (BG), which are labeled according to the ordering of Tran et al. (2009).

2.2. Measuring Galaxy Colors

To measure colors and fluxes via Source Extractor (Bertin & Arnouts 1996), we first redrizzle our data to align all images. We utilize the default HST pipeline through the calibration and flat-fielding step (flt output images), but redrizzle our data via AstroDrizzle (S. Gonzalez, W. Hack, A. Fruchter 2012) to combine our mosaic with optimized pixel resampling and astrometry. To retain resolution and to ensure detection of small-scale star forming regions, we apply the finest pixel resolution, $0''.0396/\text{pixel}$ (WFC3/UVIS), and resample the other two datasets (ACS F606W and F814W) from their native scale ($0''.05'/\text{pixel}$) to match. Resampling all images to a common resolution facilitates consistent color measure-

TABLE 1
SG1120-1202 CONSTITUENT GROUP PROPERTIES.

Index	α (J2000)	δ (J2000)	z	T (keV)	M (M_{\odot})	σ (km s^{-1})	R_{200} (kpc)	N (members)
1	11:20:07.48	-12:05:09.1	0.3522	2.2	1.3×10^{14}	303	240	28
2	11:20:13.33	-11:58:50.6	0.3707	1.7	8.0×10^{13}	406	320	27
3	11:20:22.19	-12:01:46.1	0.3712	1.8	8.9×10^{13}	580	460	54
4	11:20:10.14	-12:08:51.6	0.3694	3.0	2.3×10^{14}	576	460	47

NOTE. — Properties summarized from Gonzalez et al. (2005) and Tran et al. (2009)

ments across multi-band imaging. This resampling does not alter colors by more than 2%. We use the *final-wht-type* parameter to ensure our output weight maps are inverse variance maps as per the expected input to SExtractor (see Skelton et al. 2014 for more details).

We measure colors with SExtractor (Bertin & Arnouts 1996) in dual-image mode, which uses a reference image (here F814W) for detection and then measures fluxes in the target image (F390W or F814W). Only by using the same detection map can we directly compare colors and sizes across the filters. All pixels that are associated with a galaxy in the detection image (segmentation map) are used in calculating its flux in the target image.

We utilize published values for instrument and filter-specific fields such as zeropoints, FWHM, etc., and use default parameters for all fields except minimum detection. We adjust minimum detection area to prevent faulty detections from entering our catalogs, especially in F390W, where object sizes are substantially smaller and the background noisier. Our choice for detection area includes all galaxy members, while filtering most of the false detections such as those along the imaging boundaries and in inter-chip regions. Table 2 includes the magnitudes in F814W and F390W and half-light radius in F814W for all spectroscopically confirmed group galaxies.

2.3. Identifying UV Emission from Star Formation

We visually inspect the HST imaging to identify SG1120 members that have bright pockets of UV emission indicative of ongoing (unobscured) star formation. The O and B type stars illuminating these regions burn for ~ 30 Myrs and, while they constitute less than 7% of stellar mass (Wuyts et al. 2012), these massive stars effectively trace new sites of unobscured star formation. We note that the absence of OB-type stars does not imply that a galaxy is devoid of star formation, e.g. UV light is easily reprocessed to longer wavelengths by dust that is then detected at $24\mu\text{m}$.

J.M. and K.T. separately examined the HST imaging in the individual filters as well as in the combined RGB images (see Fig. 2, right). Group members are classified as “clumpy” if UV-bright regions exist throughout the galaxy and “smooth” if there are no such regions. Several galaxies are edge-on disks and therefore cannot be reliably classified; these are denoted as “none.”

The right side of Figure 2 shows RGB images for a sample of each visual classification, and Table 2 includes the classification for each galaxy, including “jellyfish” candidates. Because of their increased rest-frame UV flux, regions of ongoing (unobscured) star formation are visible as blue pockets of light (F390W) in the RGB images.

Approximately 30% of the supergroup have “clumpy” UV emission.

We use the F390W imaging to visually identify jellyfish candidates, which are characterized by asymmetric ultra-violet clumps with trails of knots and filaments (Smith et al. 2010). The high resolution of HST imaging allows us to visually identify such features according to the criteria used in the literature (e.g. Smith et al. 2010; Owers et al. 2012; Ebeling et al. 2014) even at $z \sim 0.37$. In Fig. 3 we include two such examples with RGB thumbnails and grayscale images of F814W and F390W. The side-by-side comparison allows the rest-frame UV emission of trails to directly contrast the underlying stellar population.

2.4. Spitzer/MIPS $24\mu\text{m}$ Fluxes

We use the *Spitzer* MIPS $24\mu\text{m}$ fluxes from Sain- tonge et al. (2008) and Tran et al. (2009). To summarize, the $24\mu\text{m}$ observations were retrieved from the *Spitzer* archive and spectral energy distributions were fit to determine the IR luminosities and corresponding star-formation rates of each source (see Saintonge et al. 2008 for details). At $z \sim 0.37$, the 80% completeness limit corresponds to $\log(\text{LIR})[\text{ergs}^{-1}] = 43.8$ or, equivalently, a star-formation rate of $3M_{\odot}$. Figure 1 shows the spatial distribution of the $24\mu\text{m}$ -detected group galaxies that also have the required F390W and F814W imaging. Following Tran et al. (2009), we attribute the IR emission to dusty star formation (contamination by active galactic nuclei is $< 3\%$).

3. RESULTS

3.1. UV Morphology Correlates with Projected Distance

As shown by Kautsch et al. (2008), the trend of increasing early-type fraction in denser environments is already established in the SG1120. We build on this morphology–density relation by examining the spatial distribution of supergroup galaxies with pockets of UV emission (“clumpy”; Fig. 2, right). We stack all four galaxy groups and find that the fraction of members with patches of UV emission (clumpy) increases with increasing distance from the group centers (Figure 4). The tendency for clumpy members to be at larger projected distances from the cores suggests that newly accreted group galaxies with UV-bright star-forming regions are extinguished as they fall into the groups. While there are a handful of members with “clumpy” emission in the group cores, their position may be due primarily to projection effects.

3.2. Color–Magnitude Diagrams (CMDs)

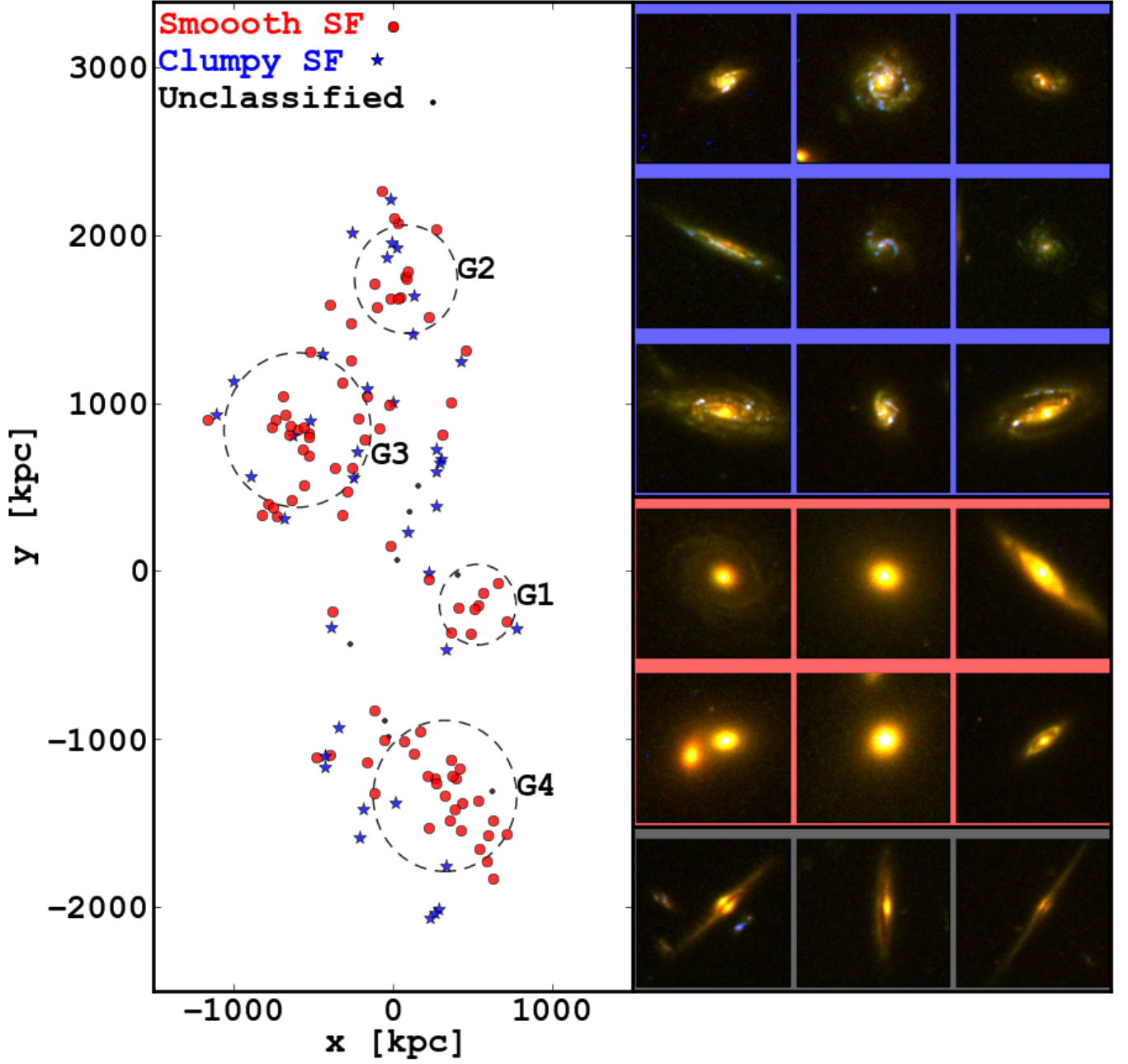


FIG. 2.— Spatial distribution of supergroup galaxies where the members are separated by visual identification of UV emission as traced by F390W. The dashed circles correspond to R_{200} for each group (see Table 1). Galaxies with pockets of UV emission in their disks are considered “clumpy” and those with smooth radial profiles are “smooth”. Examples of clumpy and smooth classifications are shown as color images (right subpanels) that are generated by combining HST F814W, F606W, and F390W. Unclassified objects are typically dust-obscured edge-on galaxies such as those in the bottom thumbnails.

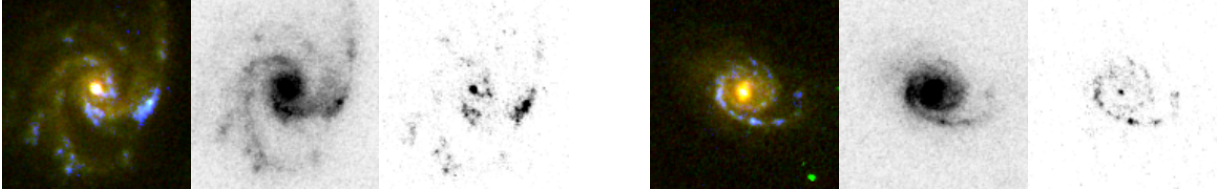


FIG. 3.— Examples of member galaxies (left: J112013.2-120345.2, right: J112014.5-115808.9), which we visually characterize as jellyfish candidates (Smith et al. 2010). Color images (left) are generated by combining HST F814W, F606W, and F390W. Grayscale images of F814W imaging (middle) and F390W imaging (right). The presence of asymmetric clumps and trails of knots and filaments serves as the defining characteristics of such galaxies. Table 2 includes labels denoting all jellyfish candidates.

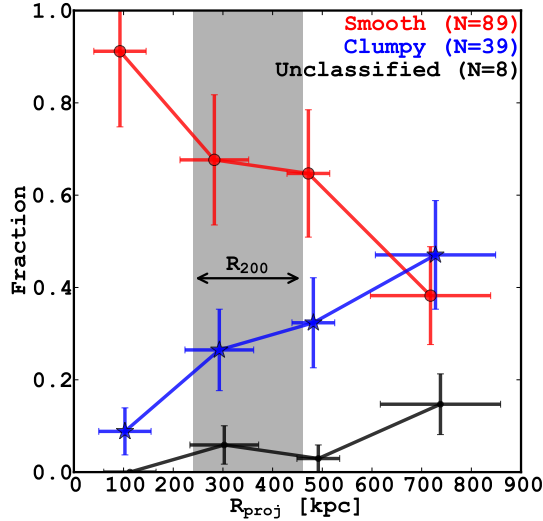


FIG. 4.— We stack the four groups in SG1120 and show the fraction of members with pockets of UV emission (clumpy) relative to those without (smooth) as a function of the projected group-centric distance. The binned points are offset by 10 kpc for clarity, and the R_{200} range for the four groups (Table 1) is shown as a vertical band. Clumpy galaxies are characterized by UV emission from ongoing star formation at extended radii and their fraction increases at larger distances from the group core. Unclassified galaxies are mostly comprised of edge-on disks, where star formation is obscured by the disk; their fraction also increases with increasing distance from the core.

CMDs are an efficient method for tracing how a galaxy evolves as its stellar population ages. As a galaxy’s star-formation rate decreases, its colors redden and move it from the blue cloud to the red sequence within the CMD. Rest-frame unobscured UV emission is particularly effective at measuring unobscured SF rates because it is generated by the youngest and most massive main-sequence OB-type stars with lifetimes of < 30 Myr. In Figure 5, we compare the $(F390W-F814W)$ distributions for different populations of supergroup members based on their IR ($24\mu\text{m}$) and UV ($F390W$) emission.

In Fig. 5 (top), we compare the color distribution of $24\mu\text{m}$ members to those that are undetected. Although $24\mu\text{m}$ and UV flux both trace star formation (Kennicutt Jr et al. 2012), the correlation with $(F390W-F814W)$ colors can be weak because UV emission is easily reprocessed by dust, which then emits in the far-infrared (Meurer et al. 1999). The 28 IR-detected supergroup galaxies above our completeness limit of $m_{F814W} > 21.2$ are about 0.3 dex bluer than the non-IR members, and a KS test confirms that the difference is significant ($> 3\sigma$).

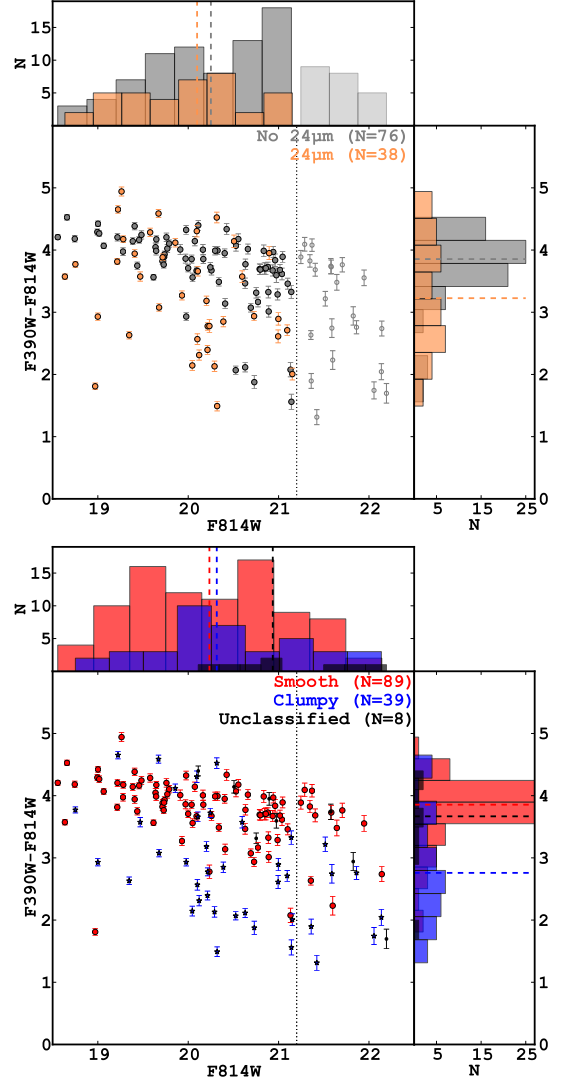


FIG. 5.— Color-magnitude diagram (top) for supergroup galaxies comparing $24\mu\text{m}$ (orange filled circles) and non-detected (gray filled circles) members; galaxies fainter than the spectroscopic completeness limit of $m_{F814W} = 21.2$ (dotted vertical line) are shown as open gray circles. Also shown is the CMD (bottom) for members with pockets of UV emission (clumpy; blue stars) or smooth profiles (smooth; red filled circles). The upper and right side histograms show the m_{814} and $(F390W-F814W)$ distributions for the different galaxy populations; the vertical dashed lines correspond to the average values. There is a larger difference in average $(F390W-F814W)$ color between clumpy vs. smooth galaxies (~ 1.0 dex) compared to $24\mu\text{m}$ vs. non- $24\mu\text{m}$ (~ 0.3 dex).

Note that while the $24\mu\text{m}$ members tend to be blue, they

also span the full range in (F390W–F814W) color and include some of the reddest galaxies.

The transition from star-forming to quiescent galaxy also usually corresponds to changes in morphology from late- to early-type (van Dokkum et al. 1998; Balogh et al. 2004; Bell et al. 2004). We compare the supergroup galaxies based on their clumpy/smooth classification (Figure 5, bottom) and find that these two populations differ in average (F390W–F814W) color by ~ 1 dex, i.e. more than three times larger than the IR vs. non-IR members. When considering all of the members, the average (F390W–F814W) colors for smooth and clumpy are 3.76 ± 0.08 and 2.79 ± 0.09 respectively; if we consider only $m_{F814W} < 21.2$, the average (F390W–F814W) are 3.81 ± 0.08 and 2.92 ± 0.09 .

To summarize, the supergroup galaxies with smooth light profiles tend to be very uniform in color, to have color shallow gradients, to be red, to have early-type morphologies, and to populate the group cores (Figs. 2 & 4, Kautsch et al. 2008). In contrast, the clumpy galaxies contain both red and blue components, span the range in galaxy color, tend to have prominent disks, and are mostly outside the group cores.

3.3. Total Galaxy Color Correlates with Projected Distance

In Fig. 6, we compare how total (F390W–F814W) color and local environment are correlated by stacking the four groups into a single system and using the projected radius (R_{proj}) from the nearest Brightest Group Galaxy (defined as the group center). The projected radius serves as a proxy for environmental density. For an analysis of how the $24\mu\text{m}$ emission depends on local environment in SG1120, we refer to Tran et al. (2009).

Supergroup galaxies in the group cores are redder than those at larger distances. A least-squares fit to the total galaxy color and projected distance for the stacked groups (Fig. 6, black line) measures a strong correlation of

$$(F390W - F814W) = 8.56 \times 10^{-4} \left(\frac{R_{\text{proj}}}{\text{kpc}} \right) + 3.82 \quad (1)$$

at $> 3\sigma$ confidence (errors in slope and offset are 2.64 and 0.12, respectively). Least-squares fits to the individual groups measure the same general trend. Figure 6 includes the error bars that represent each bin's range in R_{proj} and standard deviation in (F390W–F814W). As galaxies approach their group cores, their increasingly red (F390W–F814W) colors indicate that their star formation is quenching.

3.4. Correlations with Stellar Mass

To test if the correlation between total galaxy color and projected distance in SG1120 (see §3.3) is driven by an increasing number of massive, passive galaxies in the group cores, we compare (F390W–F814W) color to stellar mass (M_*) in Fig. 7. A least-squares fit confirms a strong correlation of

$$(F390W - F814W) = 0.95 \times \log[M_*/10^{10} M_\odot] + 3.09 \quad (2)$$

(errors in slope and offset are 0.08 and 0.06, respectively) shown as a solid line in Fig. 7: more massive

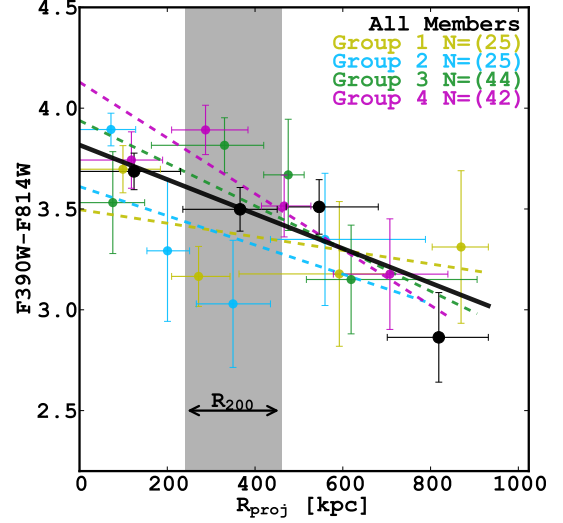


FIG. 6.— Total (F390W–F814W) color for individual supergroup galaxies compared to their projected distance (R_{proj}) for the group stack; the vertical dashed line corresponds to a projected distance of 400 kpc which is approximately R_{200} (see Table 1). We measure a strong correlation ($> 3\sigma$ confidence) between (F390W–F814W) color and projected distance (R_{proj}): members are redder in the group cores. The error bars in R_{proj} and (F390W–F814W) color represent, respectively, the bin range and standard deviation within the bin.

supergroup members have redder (F390W–F814W) colors. Although 22 galaxies are below our spectroscopic completeness limit (which we take to estimate our mass completeness), the slope of Eq. 2 changes by less than 1% when we exclude galaxies below this limit.

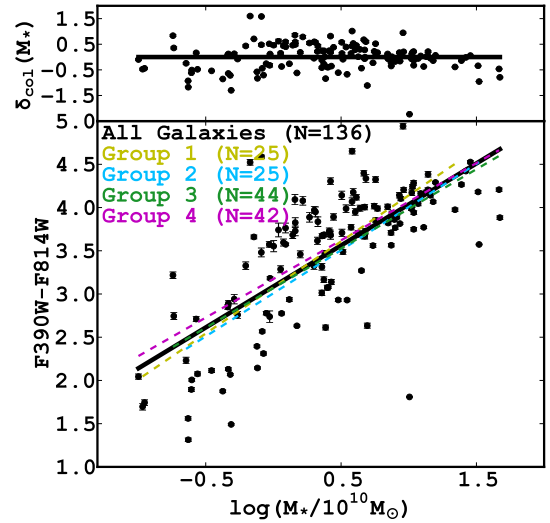


FIG. 7.— In SG1120, the total (F390W–F814W) color for individual members is tightly correlated with their stellar mass in all of the groups (bottom; colored lines are least-squares fits to the separate groups). A least-squares fit to the supergroup stack (black line) has mean residuals within ~ 0.5 dex (top). The strong correlation between (F390W–F814W) color and stellar mass is what drives the observed correlation between (F390W–F814W) and projected group distance (Fig. 6): massive supergroup galaxies tend to be red and tend to be in the group cores.

We now combine the measured relation between total galaxy color and stellar mass (Fig. 7) with the measured relation between total galaxy color and projected group

distance (Fig. 6). Mass and projected group distance correlate with a slope of $-9.02 \pm 1.95 \times 10^{-4}$, but we seek to separate the effects of these properties on total galaxy color. For each supergroup galaxy, we calculate a color deviation $\delta_{\text{col}}(M_*)$ defined as the difference between the galaxy’s measured (F390W–F814W) color and the expected value given its stellar mass from Eq. 2. Once we account for the correlation between total galaxy color and stellar mass, the trend between (F390W–F814W) color and R_{proj} disappears (Fig. 8). Least-squares fits to $\delta_{\text{col}}(M_*)$ and R_{proj} for the different galaxy populations confirm slopes within 1σ of zero (all galaxies: $-2.36 \times 10^{-5} \pm 1.84 \times 10^{-4}$), i.e., the observed trend between (F390W–F814W) color and R_{proj} is driven by stellar mass.

We test whether M_* can also explain the decreasing fraction of members with pockets of UV emission (clumpy) with decreasing group distance (Fig. 4; §3.1). The clumpy members tend to have lower stellar mass compared to the smooth members with average $\log(M_*/M_\odot)$ of 9.9 ± 0.48 and 10.7 ± 0.51 , respectively. Least-squares fits to $\delta_{\text{col}}(M_*)$ and R_{proj} of both clumpy and smooth members confirm trends consistent with zero, (clumpy: $4.39 \pm 4.48 \times 10^{-4}$, smooth: $-2.33 \pm 2.00 \times 10^{-4}$), i.e. the correlation between UV morphology and projected group distance disappears once we account for stellar mass.

To confirm that stellar mass is the key parameter driving this relation, we test whether projected group-centric distance provides an equally good explanation of the observed correlation. The correlation between color and radius is much weaker than the trend with mass. If we define $\delta_{\text{col}}(R_{\text{proj}})$ as the difference between the galaxy’s measured (F390W–F814W) color and the expected color given its R_{proj} from Eq. 1, then the residual scatter is appreciably larger (0.74 versus 0.52) and $\delta_{\text{col}}(R_{\text{proj}})$ is strongly correlated with stellar mass (slope of 0.83 ± 0.08).

We find that the primary predictor for a galaxy’s total (F390W–F814W) color and UV morphology is its stellar mass, i.e. mass-quenching (Peng et al. 2010). The increasing fraction of massive galaxies in the core is due to this environmental effect, whereas the increasing fraction of passive galaxies merely reflects mass. Our results in the group environment of SG1120 mirror results by Muzzin et al. (2012) for galaxy clusters at $z \sim 1$.

3.5. Internal Color Gradients

With high-resolution imaging from HST, we map internal color gradients at multiple half-light radii for individual supergroup galaxies. We measure the (F390W–F814W) at three circular annuli corresponding to 1.0, 1.75, and 2.5 half-light radii, where $r_{1/2}$ is measured in the F814W imaging. While other studies use more annuli to measure internal color gradients (e.g. Tamura et al. 2000; Welikala & Kneib 2012; Allen et al. 2015), we focus our analysis on three radii to ensure a robust comparison of the galaxies’ disks to their centers, while ensuring that measurement apertures are larger than the PSF for both filters.

We stack internal color gradients for the clumpy and smooth supergroup galaxies (Fig. 9) and confirm that smooth members are ~ 1 dex redder than clumpy mem-

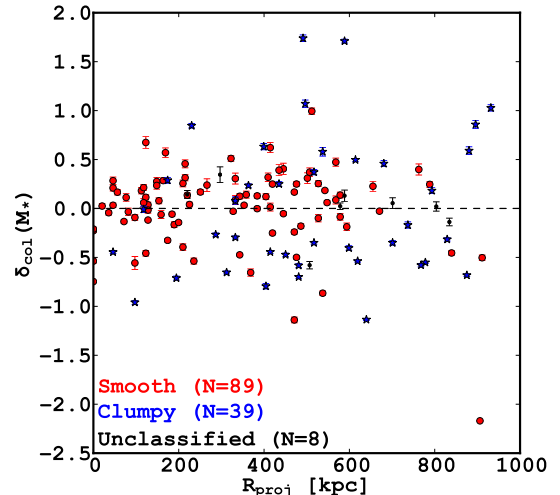


FIG. 8.— Color deviation $\delta_{\text{col}}(M_*)$ is the difference between a galaxy’s measured (F390W–F814W) color and the expected value based on its stellar mass (Eq. 2). Correcting for the stellar mass dependence removes any trend between $\delta_{\text{col}}(M_*)$ and R_{proj} ; this also holds for the clumpy (stars) and smooth (large circles) members. Least-squares fits to $\delta_{\text{col}}(M_*)$ – R_{proj} for the different galaxy populations confirm slopes within 1σ of zero (slope of $-2.36 \times 10^{-5} \pm 1.84 \times 10^{-4}$). Thus the correlation between total galaxy color and stellar mass explains the correlation between total galaxy color and projected group distance (Fig. 6).

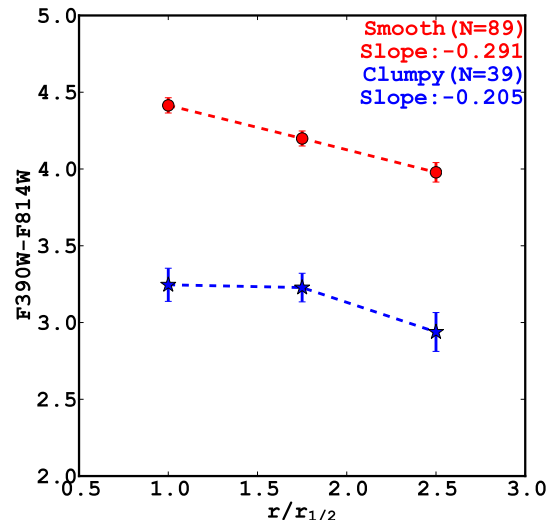


FIG. 9.— With HST’s high spatial resolution, we are able to measure internal color gradients and show the stacks for clumpy (stars) and smooth (circles) supergroup members. The smooth members are ~ 1 dex redder, and both smooth and clumpy members have shallow gradients.

bers. The average (F390W–F814W) color in each annulus is measured from the galaxy distribution (either clumpy or smooth) and the corresponding error is determined from 1000 boot-strapped realizations. The gradients of clumpy and smooth galaxies have slopes of -0.205 ± 0.104 and -0.281 ± 0.002 , respectively.

We also stack and measure internal color gradients for the $24\mu\text{m}$ -detected and non-IR members. As expected, the $24\mu\text{m}$ members are bluer (F390W–F814W) throughout their galaxy disks and centers compared to the non-IR members.

4. DISCUSSION

A number of physical mechanisms continue to be explored to explain the changes in galaxy properties with environment. Ram pressure stripping (Gunn & Gott III 1972), tidal interactions with other galaxies or with the cluster potential (Moore et al. 1998), morphological quenching (Martig et al. 2009), and environmental strangulation (Larson et al. 1980) each provide different processes that can explain the observed differences in UV emission (see Boselli & Gavazzi 2006 for a comprehensive review of such mechanisms). However, given the breadth of these studies and the range of (sometimes) contradictory conclusions, we do not attempt to solve this issue definitively here with only one system.

Instead, we consider a few clues from supergroup SG1120. The galaxies are spatially segregated by UV emission even before the cluster forms (Figs. 2 & 6), and stellar mass is the key. Most of the members with pockets of UV-bright star formation (“clumpy”) tend to be fainter (lower-mass) galaxies (Fig. 5), and a statistically significant trend between (F390W–F814W) color and stellar mass (Fig. 7, Eq. 2) drives this relation. Both results reinforce the link between increasing stellar mass and decreasing star formation (“mass-quenching”; Peng et al. 2010).

However, this is not to say that environment is unimportant (see also Cooper et al. 2010). First, there is mass-segregation in the group environment where the fraction of massive galaxies increases with decreasing R_{proj} . Second, we find for the first time group galaxies with UV tails and asymmetric UV emission (Fig. 2, top 3 rows) similar to those of jellyfish galaxies. These jellyfish candidates are interpreted as signs of shocked gas fronts in merging clusters (Owers et al. 2012) which is consistent with the incipient merger of the four X-ray luminous galaxy groups that make up SG1120. Third, the slope of the UV color-stellar mass relation in SG1120 may be different from that of the field.

The increasing fraction of UV emitting/clumpy members with increasing projected group distance (Figs. 4 & 6) mirrors the same trend for $24\mu\text{m}$ members (Tran et al. 2009). The shallow internal color gradients (Fig. 9) of both the clumpy and smooth populations suggest that quenching should happen uniformly throughout a galaxy’s disk and core once it is within $\sim 2 \times R_{200}$ of the group core (Fig. 4). The UV emitting galaxies tend to have lower stellar masses and can thus fade into the faint quiescent members that are prevalent in low-redshift clusters (De Lucia & Blaizot 2007). Alternatively, these quenched galaxies can merge to form more massive (quiescent) members in the group cores (Tran et al. 2008).

5. CONCLUSIONS

We map the UV emission in a supergroup at $z = 0.37$ by combining high-resolution imaging from the *Hubble Space Telescope* with extensive ground-based multi-band imaging and spectroscopy. SG1120 is composed of four

X-ray luminous galaxy groups that will merge and form a galaxy cluster by $z \sim 0$ (Gonzalez et al. 2005). We use WFC3/F390W and ACS/F814W imaging of supergroup galaxies to measure total (F390W–F814W) colors, visually separate UV morphology into “clumpy” and “smooth” systems, and measure internal color gradients.

These observations indicate that stellar mass is the primary predictor of UV emission in the supergroup galaxies (“mass-quenching”) while environment drives the higher fraction of massive galaxies in the group cores.

We show for the first time that several group members have UV morphologies similar to the jellyfish galaxies in massive X-ray luminous clusters. The incipient merger of the four groups in SG1120 is consistent with the interpretation that jellyfish galaxies are signs of gas shocks due to mergers.

Approximately 30% (38/128) of the visually classified supergroup galaxies have pockets of UV emission (“clumpy”; Fig. 2), a fraction that is comparable to the $24\mu\text{m}$ members (32%; Tran et al. 2009). The clumpy UV members have shallow internal (F390W–F814W) color gradients (Fig. 9).

To measure UV properties as a function of projected group distance (R_{proj}), we stack the four galaxy groups into a single system. We find that the UV emission, as measured by the total (F390W–F814W) color and by the clumpy/smooth classification, is strongly correlated with projected group distances (Figs. 4 & 6). We show that both of these trends in UV with R_{proj} are driven by the strong underlying correlation between (F390W–F814W) and stellar mass: group galaxies with UV emission tend to be lower luminosity/lower-mass members, and these systems are more common at $R_{\text{proj}} > R_{200}$ (Figs. 7 & 8).

However, we do find evidence of environmental processes. Most importantly, the higher density environment of the group cores ($R_{\text{proj}} < R_{200}$) means an increase in the fraction of members that are massive and red/smooth (mass-segregation). Also, the supergroup contains jellyfish candidates whose UV morphologies likely are shaped by interactions with the intragroup gas.

Our analysis of the supergroup galaxies indicate that stellar mass is the primary predictor of a galaxy’s UV properties (mass-quenching), but it is environment that regulates the galaxy mass distribution and shapes jellyfish galaxies.

We are grateful to J. Moustakas and D. Zaritsky for their contributions to the SG1120 data analysis and catalogs. We thank L. Alcorn, B. Forrest, and Jimmy for helpful comments on the data analysis and manuscript. J. M. and K. T. acknowledge support for Program number HST-GO-12470 provided by NASA through a grant from the Space Telescope Science Institute, which is operated by the Association of Universities for Research in Astronomy, Incorporated, under NASA contract NAS5-26555.

Facilities: VLT (VIMOS), VLT (FORIS2), Magellan (LDSS3), KPNO (Mayall 4m), HST (ACS, WFC3), SST (MIPS), CXO (ACIS), Keck (LRIS).

REFERENCES

- Abadi, M. G., Moore, B., & Bower, R. G. 1999, *Monthly Notices of the Royal Astronomical Society*, 308, 947
- Allen, R. J., Kacprzak, G. G., Spitler, L. R., et al. 2015, *ApJ*, 1

- Balogh, M. L., Baldry, I. K., Nichol, R., et al. 2004, *The Astrophysical Journal*, 615, L101
- Bekki, K., Couch, W. J., & Shioya, Y. 2002, *ApJ*, 577, 651
- Bell, E., Wolf, C., Meisenheimer, K., et al. 2004, *ApJ*, 608, 752
- Bertin, E., & Arnouts, S. 1996, *Astronomy and Astrophysics Supplement Series*, 117, 393
- Boselli, A., & Gavazzi, G. 2006, *Publications of the Astronomical Society of the Pacific*, 118, 517
- Butcher, H., & Oemler, A., Jr. 1978, *The Astrophysical Journal*, 219, 18
- Byrd, G., & Valtonen, M. 1990, *The Astrophysical Journal*, 350, 89
- Cooper, M. C., Coil, A. L., Gerke, B. F., et al. 2010, *Monthly Notices of the Royal Astronomical Society*, 409, 337
- De Lucia, G., & Blaizot, J. 2007, *Monthly Notices of the Royal Astronomical Society*, 375, 2
- Dressler, A. 1980, *The Astrophysical Journal*, 236, 351
- Dressler, A., Oemler, A., Jr., et al. 1997, *Astrophysical Journal*, 490, 577
- Ebeling, H., Stephenson, L. N., & Edge, A. C. 2014, *The Astrophysical Journal*, 781, L40
- Freeland, E., Tran, K.-V. H., Irwin, T., et al. 2011, *The Astrophysical Journal*, 742, L34
- Gallazzi, A., Bell, E. F., Wolf, C., et al. 2009, *The Astrophysical Journal*, 690, 1883
- Gonzalez, A., Tran, K.-V., Conbere, M., Zaritsky, D., & Journal, T. A. 2005, *ApJL*, 624, L73
- Gonzalez, A. H., Zaritsky, D., Dalcanton, J., & Nelson, A. 2001, *ApJS*, 137, 117
- Gunn, J., & Gott III, J. 1972, *ApJ*, 176, 1
- Hashimoto, Y., Oemler, Jr., A., Lin, H., & Tucker, D. L. 1998, *The Astrophysical Journal*, 499, 589
- Iovino, A., Cucciati, O., Scodeggio, M., et al. 2010, *Astronomy and Astrophysics*, 509, A40
- Just, D. W., Zaritsky, D., Tran, K.-V. H., et al. 2011, *The Astrophysical Journal*, 740, 54
- Kautsch, S. J., Gonzalez, A. H., Soto, C. a., et al. 2008, *The Astrophysical Journal Letters*, 688, L5
- Kennicutt Jr, R. C., Evans II, N. J., Kennicutt, R. C., & Evans, N. J. 2012, *Annual Review of Astronomy and Astrophysics*, 50, 531
- Kodama, T., Smail, I., Nakata, F., Okamura, S., & Bower, R. G. 2001, *The Astrophysical Journal*, 562, L9
- Koyama, Y., Kodama, T., Shimasaku, K., et al. 2010, *Monthly Notices of the Royal Astronomical Society*, 403, 1611
- Larson, R. B., Tinsley, B. M., & Caldwell, C. N. 1980, *The Astrophysical Journal*, 237, 692
- Martig, M., Bournaud, F., Teyssier, R., & Dekel, A. 2009, *The Astrophysical Journal*, 707, 250
- Meurer, G. R., Heckman, T. M., & Calzetti, D. 1999, *The Astrophysical Journal*, 521, 64
- Moore, B., Lake, G., & Katz, N. 1998, *The Astrophysical Journal*, 495, 139
- Muzzin, A., Wilson, G., Yee, H. K. C., et al. 2012, *The Astrophysical Journal*, 746, 188
- Owers, M. S., Couch, W. J., Nulsen, P. E. J., & Randall, S. W. 2012, *The Astrophysical Journal*, 750, L23
- Peebles, P. J. E. 1970, *The Astronomical Journal*, 75, 13
- Peng, Y.-j., Lilly, S. J., Kovač, K., et al. 2010, *The Astrophysical Journal*, 721, 193
- Postman, M., Franx, M., Cross, N. J. G., et al. 2005, *The Astronomical Journal*, 623, 721
- S. Gonzaga, W. Hack, A. Fruchter, J. M. 2012, *STScI*, 63
- Saintonge, A., Tran, K.-V. H., & Holden, B. P. 2008, *ArXiv eprints*, 685, 5
- Skelton, R. E., Whitaker, K. E., Momcheva, I. G., et al. 2014, *The Astrophysical Journal Supplement Series*, 214, 24
- Smit, M., Schrabback, T., Velander, M., et al. 2015, *Astronomy & Astrophysics*, 1
- Smith, R. J., Lucey, J. R., Price, J., Hudson, M. J., & Philipps, S. 2012, *Monthly Notices of the Royal Astronomical Society*, 419, 3167
- Smith, R. J., Lucey, J. R., Hammer, D., et al. 2010, *Monthly Notices of the Royal Astronomical Society*, 408, 1417
- Stanford, S., Eisenhardt, P. R., & Dickinson, M. 1998, *ApJ*, 10
- Tamura, N., Kobayashi, C., Arimoto, N., Kodama, T., & Ohta, K. 2000, *The Astronomical Journal*, 119, 2134
- Tonnesen, S., Bryan, G. L., & van Gorkom, J. H. 2007, *The Astrophysical Journal*, 671, 1434
- Tran, K.-V., Saintonge, A., Moustakas, J., et al. 2009, *ApJ*, 705, 809
- Tran, K.-V. H., Moustakas, J., Gonzalez, A. H., et al. 2008, *ApJ*, 17
- Tran, K.-V. H., Simard, L., Zabludoff, A. I., & Mulchaey, J. S. 2001, *ApJ*, 549, 172
- van Dokkum, P. G., Franx, M., Kelson, D. D., et al. 1998, *ApJ*, 500, 714
- Welikala, N., & Kneib, J.-p. 2012, *arXiv:1202.0494*, 13
- Wilman, D. J., Pierini, D., Tyler, K., et al. 2008, *The Astrophysical Journal*, 680, 1009
- Wuyts, S., Förster Schreiber, N. M., Genzel, R., et al. 2012, *The Astrophysical Journal*, 753, 114
- Zabludoff, A. I., & Mulchaey, J. S. 1998, *ApJ*, 496, 39

TABLE 2
OBSERVED PROPERTIES OF SUPERGROUP MEMBERS

Name ^a	z	R_{proj} (kpc)	$24\mu\text{m}^b$ (mJy)	Half-light Radius ^c F814W (kpc)	m_{814}^d	Δm_{814}	m_{390}^d	Δm_{390}	$\log[M_*/M_\odot]^e$	Clumpy
J112023.8-120326.1	0.3708	527	...	3.22	19.76	0.002	23.96	0.029	11.0	Smooth
J112019.3-120516.9	0.3545	911	...	1.45	20.69	0.002	23.77	0.028	10.4	Smooth
J112028.8-120127.6	0.3403	517	1.96	3.52	19.68	0.002	22.75	0.013	10.4	Clumpy
J112027.4-120050.0	0.3527	491	0.24	3.91	20.32	0.003	24.84	0.033	9.8	Clumpy
J112026.0-120240.4	0.3733	404	0.12	3.62	20.99	0.005	23.61	0.028	10.4	Clumpy
J112021.3-120149.6	0.3677	72	...	3.40	18.74	0.001	22.93	0.018	11.5	Smooth
J112022.2-120146.0	0.3713	0	0.13	1.44	19.72	0.001	23.60	0.021	11.7	Smooth
J112023.4-120106.7	0.3719	220	...	2.79	19.22	0.002	23.42	0.023	11.1	Smooth
J112023.9-120134.3	0.3687	148	...	1.20	21.41	0.004	25.09	0.041	10.1	Smooth
J112012.2-120736.3	0.3717	415	...	1.50	21.37	0.004	25.45	0.051	10.2	Smooth
J112011.5-120432.6	0.3693	363	0.25	2.90	20.20	0.003	23.38	0.018	10.0	Clumpy
J112009.7-120810.2	0.3672	215	...	2.23	19.41	0.001	23.79	0.032	11.1	Smooth
J112009.6-120541.1	0.3533	235	...	1.45	20.89	0.004	23.90	0.030	10.4	Smooth
J112009.3-120830.4	0.3672	128	...	2.13	19.74	0.001	23.67	0.028	10.9	Smooth
J112007.5-120509.1	0.3532	0	...	3.20	19.28	0.002	23.25	0.020	11.3	Smooth
J112007.4-120953.7	0.3671	384	...	2.20	19.46	0.001	23.62	0.024	11.1	Smooth
J112007.0-120455.7	0.3525	77	...	1.39	20.84	0.003	24.55	0.038	10.4	Smooth
J112006.8-121008.1	0.3700	471	...	0.42	21.36	0.002	23.99	0.029	10.7	Smooth
J112006.2-120920.0	0.3695	333	...	2.37	20.96	0.004	24.80	0.056	10.3	Smooth
J112024.6-120311.1	0.3731	471	...	2.17	19.00	0.001	23.42	0.017	11.4	Smooth
J112014.6-120360.0	0.3691	655	...	1.73	21.64	0.007	25.13	0.051	9.9	Smooth
J112014.5-120422.7	0.3496	589	0.20	1.93	23.32	0.023	24.92	0.038	8.3	Smooth
J112029.6-120134.0	0.3688	568	...	2.34	20.55	0.003	24.73	0.041	10.6	Smooth
J112024.3-120142.4	0.3717	164	0.10	3.58	19.58	0.002	23.86	0.026	11.0	Smooth
J112017.3-120211.5	0.3675	399	0.47	2.98	20.60	0.004	24.17	0.032	10.0	Clumpy
J112011.0-120831.0	0.3680	123	0.03	2.57	19.28	0.001	23.46	0.026	11.1	Smooth
J112008.0-120542.3	0.3511	174	...	2.02	19.62	0.001	23.18	0.018	10.9	Smooth
J112009.2-120434.0	0.3529	220	...	3.87	20.98	0.006	24.57	0.040	10.1	Unclassified
J112006.6-120937.0	0.3642	358	...	1.27	20.88	0.002	24.61	0.036	10.4	Smooth
J112006.3-121027.8	0.3742	578	...	2.41	20.26	0.002	23.93	0.034	10.7	Smooth
J112010.1-121012.6	0.3695	415	6.10	6.20	18.75	0.001	22.52	0.013	11.1	Clumpy
J112005.8-120443.4	0.3514	184	0.35	2.86	19.41	0.002	23.35	0.021	11.0	Smooth
J112005.1-120529.0	0.3501	210	...	1.36	20.77	0.003	23.94	0.033	10.4	Smooth
J112004.3-120537.7	0.3727	287	0.23	2.57	20.22	0.002	22.99	0.017	10.1	Clumpy
J112018.8-120732.1	0.3649	778	...	2.25	20.53	0.002	22.59	0.010	9.7	Clumpy
J112016.8-120906.6	0.3660	517	0.37	2.35	21.10	0.003	23.81	0.027	9.4	Clumpy
J112013.4-120747.3	0.3714	415	...	1.41	21.10	0.003	24.56	0.040	10.2	Smooth
J112006.3-120845.3	0.3724	297	...	1.86	21.58	0.004	25.32	0.079	10.0	Unclassified
J112020.6-120806.7	0.3541	839	0.26	1.75	20.73	0.002	23.66	0.024	10.1	Smooth
J112019.9-120817.7	0.3327	768	...	1.99	19.98	0.002	22.91	0.018	10.5	Clumpy
J112015.9-120847.8	0.3710	445	...	2.00	19.71	0.001	23.54	0.021	10.8	Smooth
J112012.7-120802.3	0.3535	322	...	2.34	19.98	0.002	24.30	0.032	10.8	Smooth
J112010.2-120851.6	0.3720	0	...	4.04	18.56	0.001	22.76	0.020	11.7	Smooth
J112008.8-120859.3	0.3713	113	...	2.71	19.65	0.001	23.82	0.032	11.0	Smooth
J112007.5-120857.3	0.3756	210	...	1.40	20.32	0.002	24.32	0.035	10.6	Smooth
J112009.5-120828.5	0.3688	128	0.59	3.52	19.21	0.001	23.03	0.011	10.9	Smooth
J112021.3-120154.6	0.3725	82	...	1.24	20.79	0.003	24.48	0.037	10.6	Smooth
J112011.5-120440.2	0.3509	343	...	1.41	20.80	0.003	24.48	0.027	10.4	Smooth
J112009.0-120513.2	0.3510	123	...	2.74	20.41	0.003	23.55	0.029	10.4	Smooth
J112007.7-120514.3	0.3540	36	...	2.23	19.97	0.002	23.83	0.025	10.9	Smooth
J112019.6-115920.5	0.3707	502	...	1.01	21.58	0.004	25.31	0.055	10.2	Smooth
J112018.5-120050.2	0.3758	404	...	1.52	20.93	0.004	24.61	0.030	10.4	Smooth
J112019.5-120803.9	0.3730	763	...	1.82	21.25	0.004	25.13	0.057	10.3	Smooth
J112014.2-120859.9	0.3664	312	0.69	6.27	19.00	0.002	21.93	0.014	10.5	Clumpy
J112005.1-120935.5	0.3717	445	...	1.40	21.35	0.003	25.17	0.057	10.2	Smooth
J112014.1-120415.8	0.3700	578	...	2.74	20.11	0.003	24.51	0.033	10.7	Unclassified
J112021.1-120015.0	0.3755	471	...	1.69	20.05	0.002	23.61	0.023	10.7	Smooth
J112013.0-120319.9	0.3724	701	...	2.53	21.83	0.009	24.77	0.054	9.7	Unclassified
J112008.8-120026.0	0.3867	599	...	2.77	21.36	0.007	23.26	0.022	9.4	Clumpy
J112013.3-115847.1	0.3735	20	...	2.56	19.64	0.002	23.68	0.025	11.1	Smooth
J112015.3-115708.4	0.3537	543	...	1.99	18.99	0.001	23.29	0.013	11.2	Smooth
J112013.3-115850.6	0.3706	0	0.24	2.58	18.64	0.001	22.21	0.004	11.5	Smooth
J112013.2-115841.4	0.3704	46	...	1.79	19.77	0.002	23.79	0.023	11.0	Smooth
J112010.4-120151.9	0.3771	906	2.45	2.43	18.97	0.001	20.78	0.002	11.0	Smooth
J112010.5-120220.1	0.3750	896	1.04	4.32	20.10	0.004	24.40	0.039	10.4	Clumpy
J112008.4-120012.9	0.3680	568	...	1.66	21.04	0.004	24.65	0.041	10.3	Smooth
J112014.6-115913.5	0.3711	154	...	1.43	20.63	0.003	24.41	0.030	10.6	Smooth
J112015.7-115923.7	0.3712	251	...	1.88	19.79	0.001	23.89	0.026	10.9	Smooth
J112016.6-120106.4	0.3684	476	...	2.83	19.48	0.002	23.73	0.024	11.0	Smooth
J112016.6-120058.7	0.3680	497	...	1.92	21.52	0.006	24.73	0.037	9.3	Clumpy
J112014.4-120114.0	0.3690	619	0.70	4.26	19.35	0.002	21.98	0.011	10.2	Clumpy
J112013.8-115912.2	0.3705	118	...	2.04	20.07	0.002	24.22	0.032	10.9	Smooth
J112012.7-115955.0	0.3706	333	0.13	1.99	21.15	0.004	23.16	0.015	9.4	Clumpy
J112015.5-120143.9	0.3753	512	0.16	4.77	19.26	0.002	24.20	0.033	11.0	Smooth

TABLE 2
OBSERVED PROPERTIES OF SUPERGROUP MEMBERS

J112017.8-120024.8	0.3744	537	...	3.02	21.13	0.006	23.21	0.022	9.4	Smooth
J112017.9-115942.3	0.3690	435	...	1.03	21.70	0.005	25.47	0.056	10.1	Smooth
J112008.9-120931.1	0.3721	225	...	2.45	20.04	0.002	23.89	0.024	10.8	Smooth
J112008.9-120819.7	0.3683	189	...	1.62	20.34	0.002	23.83	0.029	10.5	Smooth
J112009.4-120906.4	0.3673	97	...	2.62	20.09	0.001	23.76	0.032	10.7	Smooth
J112009.7-120920.0	0.3652	148	...	1.51	20.40	0.002	24.35	0.038	10.6	Smooth
J112010.7-121104.0	0.3500	681	0.53	4.63	19.86	0.002	23.98	0.031	10.6	Clumpy
J112010.0-120601.5	0.3580	333	...	1.72	21.86	0.005	24.62	0.040	9.7	Clumpy
J112011.0-121108.5	0.3510	701	...	2.59	20.63	0.003	22.74	0.022	9.5	Clumpy
J112010.9-120836.3	0.3680	97	...	0.86	22.14	0.005	24.88	0.066	10.0	Smooth
J112011.5-120928.7	0.3692	215	...	2.65	20.94	0.003	24.91	0.040	10.3	Smooth
J112011.5-120828.3	0.3702	159	...	1.90	20.99	0.003	24.28	0.040	10.1	Smooth
J112011.3-121114.2	0.3667	737	...	2.42	22.06	0.009	23.80	0.031	9.0	Clumpy
J112015.1-120722.9	0.3720	589	0.17	3.43	20.90	0.004	24.85	0.057	10.3	Unclassified
J112014.8-120742.3	0.3692	507	...	2.35	20.75	0.003	24.07	0.038	10.4	Unclassified
J112015.1-120746.3	0.3720	507	...	2.24	20.53	0.003	24.60	0.043	10.6	Smooth
J112015.9-120712.7	0.3706	671	...	2.23	19.07	0.001	23.13	0.016	11.2	Smooth
J112016.5-120812.8	0.3713	527	...	2.30	20.63	0.003	24.09	0.037	10.4	Smooth
J112017.1-120940.2	0.3512	589	0.46	4.90	19.67	0.002	24.26	0.019	9.9	Clumpy
J112017.9-120554.8	0.3900	834	...	3.15	22.19	0.012	23.89	0.037	9.0	Unclassified
J112019.5-120536.0	0.3746	932	1.27	4.98	19.22	0.001	23.88	0.032	10.6	Clumpy
J112020.0-120805.8	0.3449	793	...	2.27	22.14	0.008	24.18	0.029	9.0	Clumpy
J112010.9-120234.9	0.3744	829	0.61	5.16	20.10	0.004	22.67	0.017	9.9	Clumpy
J112009.6-120114.1	0.3698	788	...	2.14	20.16	0.003	24.17	0.032	10.7	Smooth
J112010.9-115752.1	0.3692	353	...	3.06	19.02	0.001	23.28	0.019	11.4	Smooth
J112023.3-120329.7	0.3758	537	...	2.89	21.14	0.005	24.47	0.044	9.8	Clumpy
J112010.5-120223.8	0.3744	880	...	3.07	21.59	0.011	24.33	0.038	9.3	Clumpy
J112010.9-120207.8	0.3770	875	...	3.98	20.73	0.005	22.61	0.012	9.6	Clumpy
J112010.9-120315.3	0.3497	640	0.21	2.68	20.32	0.003	21.81	0.009	9.7	Clumpy ^f
J112011.5-115935.2	0.3681	266	...	0.84	21.95	0.006	25.50	0.064	10.0	Smooth
J112012.4-120250.3	0.3747	804	0.17	3.43	20.51	0.004	24.65	0.048	10.5	Unclassified
J112012.6-115910.6	0.3712	118	...	1.89	20.24	0.002	23.97	0.032	10.7	Clumpy
J112013.2-120345.2	0.3684	614	0.62	6.39	19.47	0.003	23.04	0.015	10.1	Clumpy ^f
J112014.0-115744.5	0.3339	343	0.07	2.82	19.93	0.003	23.20	0.016	10.7	Smooth
J112014.0-115913.1	0.3692	128	...	2.02	20.17	0.002	24.02	0.032	10.8	Smooth
J112014.1-115814.3	0.3325	195	...	3.72	21.14	0.007	22.70	0.019	9.4	Clumpy
J112014.5-115808.9	0.3742	230	0.19	3.47	20.11	0.003	23.77	0.022	9.9	Clumpy ^f
J112014.3-115739.8	0.3713	369	...	3.76	21.60	0.011	23.83	0.036	9.4	Smooth
J112014.7-120117.2	0.3701	594	...	1.77	20.89	0.004	24.21	0.038	10.3	Smooth
J112014.6-115718.1	0.3741	481	0.27	4.27	20.05	0.003	22.19	0.013	9.9	Clumpy
J112014.9-115825.6	0.3736	174	0.12	3.14	21.00	0.004	23.89	0.030	9.7	Clumpy
J112015.9-115855.1	0.3692	200	...	1.79	19.73	0.001	23.49	0.021	10.9	Smooth
J112016.8-120156.3	0.3712	420	...	2.41	19.44	0.002	23.18	0.019	11.0	Smooth
J112017.3-120132.4	0.3711	384	...	1.81	19.65	0.002	23.63	0.022	11.0	Smooth
J112017.6-120241.1	0.3338	450	1.04	4.53	20.29	0.003	22.42	0.016	9.7	Clumpy
J112017.7-115757.2	0.3549	435	0.39	2.86	20.39	0.003	23.24	0.026	9.7	Clumpy
J112018.2-120256.8	0.3761	476	0.10	6.56	20.23	0.005	23.01	0.019	9.9	Smooth
J112017.8-120230.5	0.3708	410	...	1.55	20.84	0.004	24.82	0.043	10.5	Smooth
J112018.5-120324.3	0.3737	578	...	4.41	19.91	0.003	23.92	0.030	10.8	Smooth
J112019.2-120230.7	0.3701	328	...	1.89	19.73	0.002	23.62	0.020	10.9	Smooth
J112020.1-120017.2	0.3692	481	0.19	3.70	20.12	0.003	22.43	0.019	9.9	Clumpy
J112021.6-120143.2	0.3716	46	...	1.37	20.66	0.003	24.68	0.031	10.7	Smooth
J112021.1-120135.5	0.3677	97	...	2.84	21.42	0.007	22.74	0.019	9.4	Clumpy ^f
J112021.3-120215.6	0.3735	169	...	2.48	20.43	0.003	24.76	0.048	10.7	Smooth
J112021.8-120208.2	0.3712	118	...	1.67	20.86	0.004	24.57	0.041	10.5	Smooth
J112022.7-120307.5	0.3742	420	...	3.82	18.66	0.001	23.19	0.020	11.5	Smooth
J112021.7-120250.4	0.3686	333	...	1.64	21.02	0.003	24.70	0.046	10.4	Smooth
J112022.6-120153.2	0.3455	46	0.90	2.45	20.21	0.002	22.61	0.016	9.9	Clumpy ^f
J112022.9-120151.4	0.3714	56	...	0.99	20.30	0.002	24.29	0.028	10.8	Smooth
J112022.7-120141.4	0.3708	46	...	1.10	21.04	0.003	24.94	0.037	10.4	Smooth
J112023.2-120127.6	0.3731	123	...	1.26	21.29	0.004	25.38	0.059	10.2	Smooth
J112025.0-120324.1	0.3723	548	...	2.35	19.39	0.001	23.53	0.022	11.2	Smooth
J112024.2-120316.1	0.3703	486	...	1.61	20.00	0.001	23.71	0.026	10.9	Smooth

^a Names follow the SDSS format: JHHMMSS.s \pm DDMMSS.s for R.A. and decl. in sexagesimal units.

^b Errors corresponding to adopting different conversion factors for $F_{24\mu m}$ to $F_{8-1000\mu m}$ are $\sim 10 - 20\%$.

^c For galaxies with $r_{1/2} > 1$ kpc, Source Extractor measurements of the error on their spheroid radii are $\sim 1 - 8\%$.

^d Magnitudes are observed-frame.

^e See Tran et al. (2009) for errors in mass calculation.

^f Jellyfish candidate